

Flow Characteristics of Bulb Tubular Turbine Based on Solid-liquid Two-phase Flow Model

Q. Li^{1†}, F. Zhou^{1,2} and Q. Wang³

¹*School of Energy and Power Engineering, Lanzhou University of Technology, Lanzhou, Gansu Province, 730050, China*

²*Gansu Provincial Key Laboratory of Solar Power Generation Systems, Jiuquan Vocational and Technical College, Jiuquan, 735000, China*

³*Huaneng (Gansu) New Energy Co., Ltd., Lanzhou, Gansu Province, 730070, China*

†*Corresponding Author Email: Lqfy@lut.edu.cn*

ABSTRACT

This study examines the operational efficiency of a bulb tubular turbine under solid-liquid two-phase (SLTP) flow conditions. By employing the Euler-Euler method, the characteristics of SLTP flow in the turbine with different solid particle diameters were analyzed. The research findings demonstrate that the increase in solid particle diameter from 0.01 mm to 0.15 mm decreases the maximum liquid phase velocity in the XY plane by approximately 0.26%. The introduction of solid particles results in increased likelihood of cavitation and vortices in the draft tube region, leading to diminished energy recovery efficiency in this area. Within the impeller domain, regions with high solid particle concentration are predominantly located on the blade front hub and inlet edge, while the blade's rear side exhibits an overall higher concentration. Further analysis reveals a positive correlation between blade velocity/concentration distribution and the diameter of solid particles. Furthermore, particle size has a significant impact on the solid phase trajectory and solid phase velocity in the draft tube area. Particles with larger diameters tend to move in more irregular and chaotic patterns, promoting the formation of vortices in the draft tube region. Notably, while the velocity of the solid phase at the draft tube inlet decreases with increasing particle size, the velocity fluctuations within the draft tube become more pronounced. Among the different flow components of the hydraulic turbine, the wear severity follows a descending order: the blade region experiences the highest wear, followed by the runner chamber, guide vane area, and draft tube region. Additionally, the diameter of the solid phase shows a positive correlation with both the wear area and the maximum wear rate in the runner chamber, blade region, and guide vane area, whereas it demonstrates a negative correlation with wear in the draft tube region.

Article History

Received December 23, 2024

Revised February 27, 2025

Accepted March 13, 2025

Available online June 6, 2025

Keywords:

Tubular turbine

Solid-liquid two-phase flow

Pressure pulsation

Particle wear

Fluid machinery

1. INTRODUCTION

Against the backdrop of economic globalization, there has been a sharp increase in human energy demand. However, the extensive use of traditional fossil fuels has led to numerous environmental issues. Therefore, it is essential to prioritize the advancement and adoption of renewable energy solutions. Within the spectrum of clean energy alternatives, hydroelectric power stands out as one of the most reliable and well-established technologies (Fonkenell 2003; Guénette et al., 2012). With medium- to high-head hydropower resources gradually saturating, the industry has shifted its focus toward the development of low-head turbine units. Bulb tubular turbines, as the

preferred hydraulic machinery for low-head, high-flow hydroelectric plants, have garnered favor because of their compact structure, high efficiency, and strong adaptability (Kang et al., 2016; Li et al., 2022; Li et al., 2023a). Their low-head and high-flow characteristics impart exceptionally high specific speeds to the unit, surpassing the peaks of 1000. This implies that under equivalent head and output conditions, the impeller diameter of a bulb tubular turbine can be reduced by approximately 15% compared to that of an axial flow turbine, effectively lowering the initial construction costs of the plant. Furthermore, the radial design employed by bulb tubular turbines provides a smooth passage for fish, perfectly aligning with contemporary fish-friendly unit design

NOMENCLATURE			
A	amplitude of oscillation	F_y	component of the resultant pressure force acting on the lower side
a	cylinder diameter	h	height
C_p	pressure coefficient	i	time index during navigation
d	jet diameter	j	space index
D	cylinder diameter	α	angle of attack
h	penetration depth	γ	dummy variable
V	jet velocity		

concepts and contributing to the harmonious coexistence of economy and ecology (Brezovec et al., 2020; Coulaud et al., 2020; Li et al., 2024).

To enhance the operational efficiency and stability of bulb tubular turbine units, Li et al. (2018, 2019) delved into the dynamic behaviors of internal flow fields, power characteristic performances, internal vortex evolution mechanisms, and inherent correlation laws of external characteristic performance based on experimental data within the framework of real unit coordination relationships. Zhao et al. (2013) narrowed their research focus by analyzing how specific geometric parameters—such as the leading edge, trailing edge, and blade shape and position—affect the internal flow dynamics and energy performance of bulb turbines. In a separate study, Wilhelm et al. (2016) applied RANS and large-eddy simulation techniques to model the flow behavior of bulb tubular turbines at two distinct operating conditions. Their findings highlighted the presence of turbulence near the draft tube wall and central area, identifying it as a key contributor to head loss. Moreover, Young-Do Choi & Son (2012) performed numerical simulation analyses on microbulb turbines within an extremely low specific speed range, showing that optimizing the guide vane setting angle and blade installation angle layout can notably enhance turbine performance.

During the operation of hydroelectric power plants, water turbines face complex operational environments, particularly dynamic challenges posed by the interaction between water flow and solid particles. This interaction significantly affects performance and stability. Engineers have adopted diverse strategies to address the challenges posed by complex flow environments on turbine performance. They optimized designs and enhanced blade performance to alleviate the negative impacts of solid particles on the internal flow channels and improve turbine stability under harsh conditions. However, researchers have explicitly stated that effective management of small hydropower plants is a crucial factor in gradually improving turbine efficiency over time. A sharp increase in the particle content of water during flood seasons often leads to severe erosion and wear of turbines. This wear phenomenon becomes particularly pronounced after several years of turbine operation, subsequently causing a significant decline in turbine performance (Lemay et al., 2015; Litvinov et al., 2018; Pereira et al., 2019). Han et al. (2018a; 2018b) conducted unsteady numerical simulations of sand-laden water flow through the clearance between the guide vanes of water turbines. By employing the DPM model in FLUENT software alongside a simplified representation of the clearance flow between the turbine's

moving guide vanes, comprehensive numerical simulations were conducted to evaluate the distribution of average wear rates on the upper and lower surfaces of the clearance across various operating conditions, extensively examining the regularity of erosion and its specific occurrence locations. Yi and Liu (2013) demonstrated in their investigation of the hydraulic transport properties of solid-liquid two-phase (SLTP) flow in vortex pumps that, at a fixed particle concentration, pump efficiency and head tend to decline as particle size increases. In a related study, Li et al. (2022) employed a combination of numerical simulations and experimental validation to thoroughly examine the two-phase flow behavior and wear patterns in particle pumps with mixed particle sizes. Their results indicated that, under identical mass concentration conditions, increasing the proportion of small particles led to a notable enhancement in both the head and efficiency of the centrifugal pump. Furthermore, compared to the transport of single-sized large particles, mixed particle sizes resulted in more intricate variations in the wear distribution across flow components. Thapa et al. (2012) focused on mixed-flow hydro turbines, developed an appropriate erosion prediction model, and derived an improved empirical formula for quantitatively assessing the sediment erosion conditions of mixed-flow impellers under specific operating conditions. To validate the effectiveness of the formula, the predicted results were comprehensively compared with field-measured test data, demonstrating a high degree of consistency and confirming the accuracy and reliability of the formula. Chen et al. (2019) conducted an in-depth analysis to explore the specific impact of particle motion within pipelines on the flow characteristics of slurries. Their results indicated a significant relationship between particle sphericity, collision frequency, and energy loss inside the pipeline, where lower particle sphericity corresponded to a higher collision frequency and energy loss within the pipeline. Furthermore, the works of Yi et al. (2012) and Yi et al. (2022) deepened our understanding in this field. They discovered that, as the thickness of the ceramic slurry pump blades gradually increased, the entry angle of the solid particles correspondingly increased, directly resulting in an expansion of the particle trajectory envelope angle. This change plays a positive role in alleviating wear on the leading and pressure surfaces of the blades. They also employed the Euler-Euler method to comprehensively simulate long- and short-bladed hydro turbines operating in sediment-containing water, successfully predicting the wear intensity at different sediment concentrations during a one-year operational duration. Zhou et al. (2023) numerically simulated the solid-liquid two-phase flow characteristics and wear

behavior of a hydraulic turbine in a highly sandy river using ANSYS CFX software relying on the Euler–Euler two-phase flow model. The results show that an increase in both the sand particle diameter and volume fraction significantly increases the wear area, and the accumulation of sand particles in the direction of gravity in the localized area exacerbates the flow channel wear. The prediction shows that the total wear of Francis turbine long and short blades in one year of operation is 9.09 mm and 2.33 mm, respectively, which seriously affects the stability of the unit.

In SLTP flow conditions, the presence of solid particles not only significantly alters the flow field structure but also induces flow separation phenomena, enhances turbulent intensity, and exacerbates wear issues, all of which have profound effects on the operational efficiency and lifespan of hydro turbines. Therefore, the characteristics of SLTP flow are considered key factors affecting the performance of bulb tubular turbines. Given its importance, an in-depth exploration of the specific effects of SLTP flow on the flow characteristics of bulb tubular turbines has far-reaching theoretical contributions and potential engineering applications, as it is rooted in a SLTP flow model and involves a comprehensive and systematic analysis of the flow characteristics of bulb tubular turbines in SLTP flow environments through the integrated use of numerical simulations and experimental validation. During the research process, key parameters, such as different solid particle concentrations, particle sizes, and flow velocities, were carefully examined to reveal the influence of these parameters on the flow field structure, pressure distribution, and overall hydraulic performance within the turbine. By thoroughly dissecting these influencing mechanisms, this study aims to provide a scientific basis for optimizing the design of bulb tubular turbines, thereby enhancing their operational performance and stability in complex flow environments.

2. PHYSICAL MODEL AND NUMERICAL METHODS

2.1 Structural Parameters

The physical model selected for this study was a bulb tubular turbine used in a power plant. This turbine operates at a rated speed of $n = 85.71 \text{ r/min}$, with a rated head of $H = 6.85 \text{ m}$ and a rated flow rate of $Q = 246.74 \text{ m}^3/\text{s}$ under nominal operating conditions. Because of the structural characteristics of the intake components of the bulb tubular turbine, the inlet was designed in a straight cone shape, whereas the outlet adopted a diffuser form. This design minimizes changes in the flow direction as water passes through, effectively reducing hydraulic losses and ensuring a wide and efficient operational range. The design parameters in Table 1.

2.2 Model Construction

The three-dimensional modeling software Pro/E was employed to create a comprehensive model of the entire flow passage in the bulb tubular turbine unit. The model comprises five key components: the inlet passage, bulb body, guide vanes, runner, and draft tube. During the modeling process, the actual turbine was fully modeled with an overall length of 52,300 mm. The model was

Table 1 Parameters of bulb tubular turbine

Parameter	Number
Runner blade count	4
Movable guide vane blade count	16
Movable guide vane height	3060 mm
Diameter of the runner	5500 mm
Runner blade angle range	7~43°
Guide vane angle range	14~75°
Draft tube inlet diameter	5588 mm
Draft tube outlet width	9305 mm
Rated machine speed	85.71 r/min
Rated head	6.85 m
Rated flow rate	246.74 m ³ /s

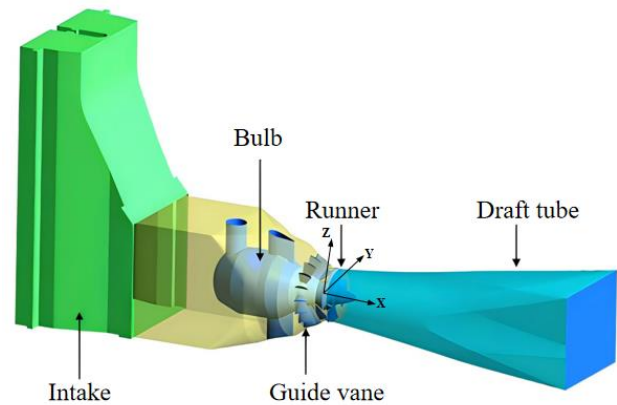


Fig. 1 3D water body diagram of a tubular turbine

based on the hub center of the runner as the reference origin, using the X-axis as the reference axis. The front half of the unit had a length of 24,800 mm, whereas the rear half had a length of 27,500 mm. Owing to the large size of the unit, precision and attention to detail are crucial during the modeling process. Modeling was performed based on hydraulic drawings and flow control dimensions provided by the power station, resulting in the overall flow-through components, as shown in Fig. 1.

2.3 Grid Division

ANSYS ICEM was used for the structured meshing of the bulb through-flow turbine because of the simple and regular structure of the inlet runner, bulb body, and tailpipe. By slicing the fluid domain into blocks using an O-mesh and topologizing it, high-quality low-number meshes were generated. Figure 2 illustrates a schematic of the local meshes of the inlet runner, bulb body, and tailpipe. However, a bulb through-flow turbine is a high-specific-speed model with a flatter blade shape, and the individual runners of the runner blades are difficult to clearly distinguish. In addition, the rims of the paddle blades and the outlet edges of the runner blades are thin, resulting in a structured mesh that is difficult to handle, has low mesh quality, and is prone to breakage. Therefore, an unstructured mesh was used for the processing. However, a large number of rotors and guide vanes must be meshed during the unit concatenation characterization study, and the use of unstructured meshing helps reduce the workload.

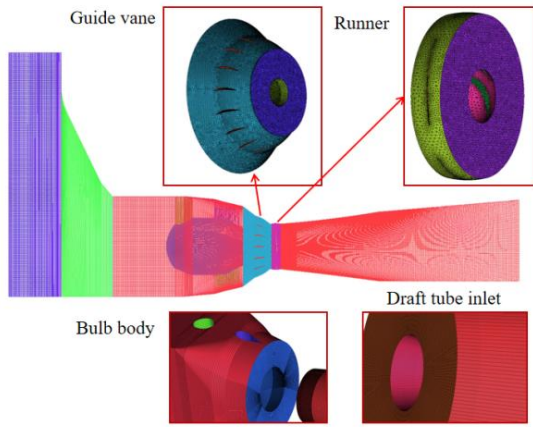


Fig. 2 Turbine computational domain mesh

Table 2 Grid-independent verification

Scheme	Total Mesh (10^6)	η/η_o	v_{max}/v
Mesh1	6.1600	4.220	0.88
Mesh2	6.7524	3.810	0.87
Mesh3	7.6245	3.460	0.85
Mesh4	8.5000	3.424	0.84
Mesh5	9.2467	3.421	0.83
Mesh6	10.259	3.420	0.83

To further optimize the mesh, local encryption of the boundary layer was performed in the near-wall region. The first layer height of the rotor blade wall mesh is configured at 0.04 mm, while the first layer height for the remaining wall meshes is set to 0.08 mm. A uniform growth rate of 1.12 is applied across all regions.

During the meshing process, to ensure the accuracy of the numerical computation results and eliminate the potential effects of the mesh density on the results, a thorough grid independence verification is essential before delving into an in-depth investigation of the bulb tubular turbine. Considering a blade angle setting of 22° for the runner and coordinated guide vane angles adjusted to 58° , a comprehensive comparative study was conducted between the computational efficiency and actual operational efficiency. Six different mesh configuration schemes were used, as listed in Table 2. Through rigorous numerical computations, it was observed that beyond a threshold of 8.5 million mesh elements, the deviation between the efficiency (η) obtained from numerical calculations and the efficiency of actual unit operation (η_o) tends to stabilize, showing no significant variation, and the ratio of the maximum flow velocity (v_{max}) to the circumferential velocity ($v = \pi nD/60$) of the rotor obtained from the calculation results does not fluctuate significantly. Based on this observation and a detailed computational analysis, the optimal mesh element count was determined to be approximately 8.5 million to ensure the accuracy and reliability of the numerical computations.

In nonstationary calculations, the selection of the time step is crucial for the accuracy of the calculation results. To ensure the accuracy of the calculation, the sensitivity of the time step was analyzed by monitoring the change in

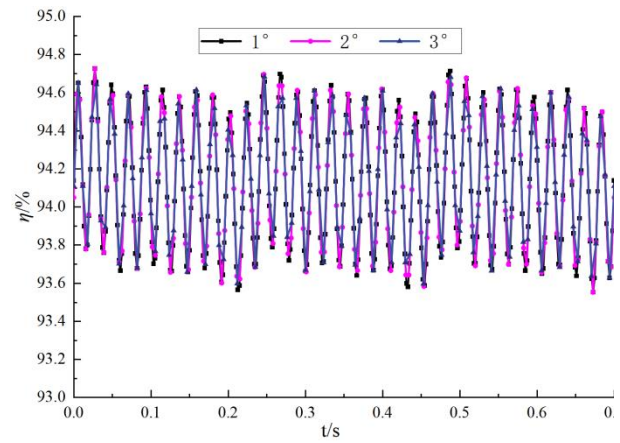


Fig. 3 Verification of time-step irrelevance

the efficiency of the hydraulic turbine at rotor rotation angles of 1° , 2° , and 3° . It has been shown that in transient calculations, it is usually necessary to simulate rotor rotation for five to eight cycles to obtain a stable numerical solution; therefore, six complete rotor rotation cycles were set up in this study for computational validation. As shown in Fig. 3, the efficiency trends of the turbine were highly consistent under different time steps, indicating that the choice of the time step did not significantly affect the calculation results. Based on the comprehensive consideration of computational accuracy and computational resources, the time step $\Delta t = 0.00583362$ s, which corresponds to the time required for the impeller to rotate by 3° , was finally selected as the nonstationary computational setting in this study. This choice ensures a balance between computational efficiency and reliability by effectively controlling computational cost while guaranteeing computational accuracy.

2.4 Boundary Conditions and Two-Phase Flow Settings

In the simulation of solid-liquid two-phase (SLTP) flow, the following configurations and strategies were implemented: Under clear water conditions, the fluid medium was defined as water at a temperature of 298 K. The flow was treated as incompressible with a constant density, based on operational parameters. A mass flow inlet boundary condition was applied, while the outlet was configured for free outflow (Dryden et al., 2016; Li et al., 2023b). For the numerical approach, the Eulerian-Eulerian method with a particle non-uniform phase model was selected to accurately capture the two-phase flow dynamics. To better reflect real-world conditions, the rotor region was designated as a rotating domain, while the rest of the system was treated as a stationary domain. Computational settings included a guide vane opening of 58° and a blade opening of 22° . For the solid phase, particles with a density of 2650 kg/m^3 and varying diameters (0.01 mm, 0.05 mm, and 0.15 mm) were considered. The particle diameters were non-dimensionalized using the average diameter of fine sand ($d_{ref} = 0.1 \text{ mm}$) as the reference length.

$$d^* = \frac{d}{d_{ref}} \quad (1)$$

where d is the particle diameter, $d_{ref}=0.1$ mm is the average diameter of fine sand, and d^* is the dimensionless particle diameter.

A zero-equation model was used to simulate the discrete phase, and a Gidaspow model was chosen for the tracer phase. For the turbulent dissipative force, the Favre-averaged drag force model was selected, and the dissipation factor was set to 0.9. The turbulent transport model employed the Sato-enhanced viscosity model, while the SIMPLEC algorithm was utilized to address pressure–velocity coupling (Xie et al., 2023). Regarding momentum exchange, the tug force was primarily considered, with the Schiller–Naumann function model selected for simulation. The effects of lift force, virtual mass force, and wall lubrication force were neglected. For boundary conditions, the solid phase was assigned a free-slip condition, whereas the liquid phase was modeled with a no-slip condition. To ensure computational accuracy, a standard convergence criterion of 1.0×10^{-5} was applied, and an appropriate time step of 0.00583362 s (equivalent to a 3° rotation of the rotor) was adopted. In the transient simulation, six rotor rotation cycles were computed, resulting in a total solution time of 4.20022 s, with a convergence criterion of 1×10^{-4} . The computation strategy involved an initial steady-state simulation to obtain the flow field, followed by a transient simulation of the solid-liquid two-phase (SLTP) flow using the steady-state results as the initial condition. This approach enhances the accuracy of simulating SLTP flow characteristics under realistic operating conditions.

2.5 Numerical Method Verification

To ensure that the numerical computations were in accordance with the actual flow conditions, we considered a blade angle of 22° and selected seven operational points with guide vane angles ranging from 50° to 62° . Numerical calculations were performed at these points, and the efficiency curves obtained were compared with the efficiency results from the actual unit tests and model turbine tests. This comparison validated the reliability of the numerical simulations conducted in this study.

The efficiency trends derived from the numerical simulations exhibited an initial rise followed by a decline, consistent with the outcomes observed in the actual unit tests. In particular, at a guide vane angle setting of 52° , although the efficiency difference between the numerical calculations and model test experiments reached its maximum value, the deviation remained within an acceptable error margin (not exceeding 6%), thereby validating the accuracy and reliability of the numerical computations. As shown in Fig. 4, the efficiency values recorded during the actual unit tests were higher than the numerical calculation results. This phenomenon can be attributed to the increase in local hydraulic losses as the turbine model was scaled down proportionally. In addition, the efficiency values obtained from the numerical calculations slightly outperformed the performance of the turbine model on the test stand. Through an in-depth comparison and analysis of the experimental data and numerical computation results, the hydraulic model developed in this study demonstrated a high level of precision, whereas the numerical computation methods

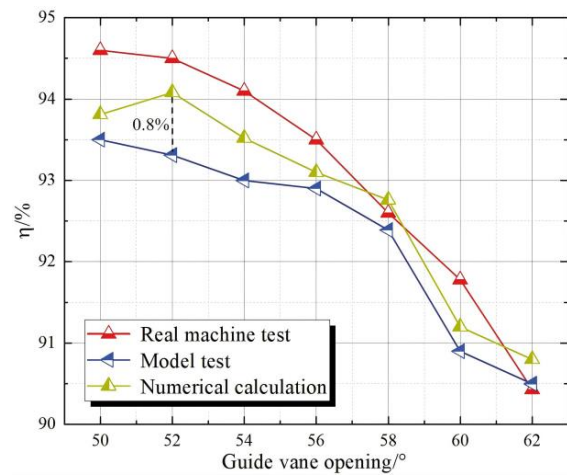


Fig. 4 Accuracy verification of numerical methods

and turbulence model employed exhibited strong credibility and reliability.

3. RESULTS OF CALCULATIONS AND ANALYSIS

3.1 Analysis of Flow Velocity in XY Plane of Water Turbine

Figure 5 illustrates the distribution of the liquid-phase velocities on the XY plane of the bulb tubular turbine. The graph reveals a roughly symmetric distribution of liquid-phase velocities, with the guide vane region, runner area, and near-wall section of the draft tube being the main locations of higher liquid-phase velocities. This phenomenon is primarily attributed to the contraction-flow channel characteristics on both sides of the bulb structure. As water flows through these areas, the gradual reduction in the channel area causes water convergence, leading to a gradual increase in the liquid-phase velocity. Specifically, within the runner area, the influence of channel area variations is compounded by the centrifugal force generated by high-speed rotation, resulting in peak liquid-phase velocities in this region. Additionally, with an increase in solid particle diameter (ranging from 0.01 mm to 0.15 mm), a slight downward trend in maximum liquid-phase velocity on the XY plane is observed—from 19.832 m/s to 19.827 m/s—representing a decrease of approximately 0.26%. This observed variation can be attributed to multiple effects stemming from the increase in particle size in the SLTP flow system. First, as the diameter of the solid particles increases, the interaction between the solid and liquid phases significantly intensifies, causing heightened collision and friction effects between particles and the fluid, thereby generating additional flow resistance that decelerates the water flow speed. Second, based on the fundamental principle of momentum conservation, when solid particles enter a flowing system at a certain velocity, the liquid-phase momentum is redistributed. Larger particles possessing greater inertia consume more kinetic energy during flow, consequently leading to a decrease in the liquid-phase velocity. Furthermore, the presence of larger solid particles in the channel creates an obstructive effect, occupying some of the effective flow space and further

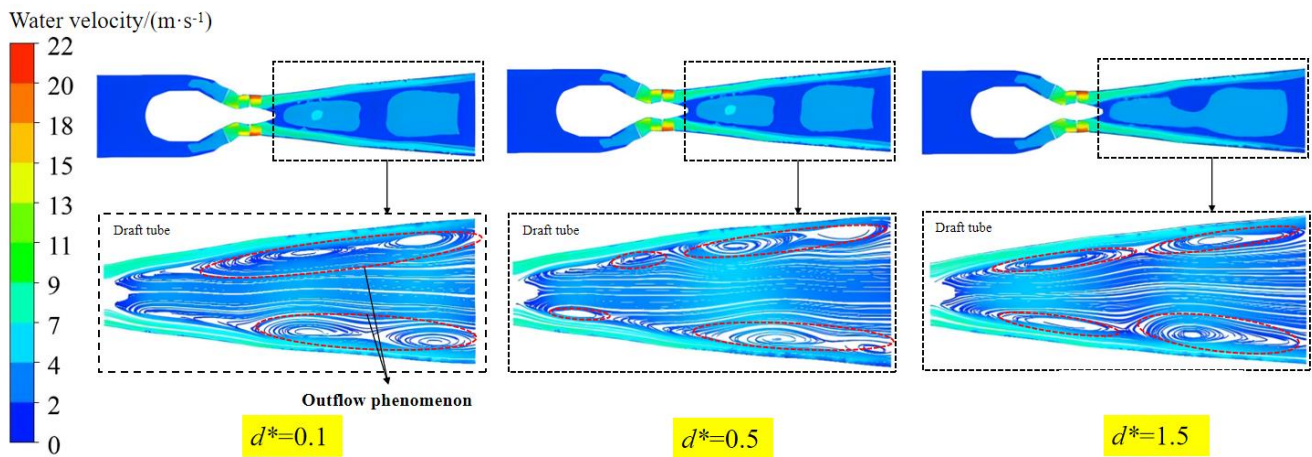


Fig. 5 XY plane liquid phase velocity distribution diagram

increasing the local flow resistance. Additionally, the existence of solid particles may impact local turbulent structures, resulting in increased turbulence losses and further reductions in liquid-phase velocity.

Subsequently, as water flows into the draft tube, owing to the significantly greater inertia of solid particles, their shear deformation capability is much lower than that of clean water, and they exhibit poor adaptability to the channel, often leading to flow separation. Furthermore, the collisions, friction, and rotations of particles within the turbine flow passage can disturb the liquid-phase flow, intensifying water pulsation and vortex formation, thereby affecting the flow regime. It is evident that with an increase in the solid particle diameter, the streamline velocity in the XY section of the draft tube decreased slightly from 21.8214 m/s to 21.7966 m/s. This reduction is attributed to larger solid particle diameters resulting in higher inertia forces, leading to increased momentum exchange with the liquid phase and causing a decrease in liquid phase velocity. Moreover, under different solid particle diameters, varying degrees of vortices are observed near the walls of the draft tube. At the draft tube exit, flow separation occurs, resulting in greater hydraulic losses, which lead to issues such as unit vibration and lower operational efficiency.

3.2 Flow Analysis in Runner Region

Figure 6 illustrates the pressure distribution along the streamline direction at the midsection of the runner blades for varying solid particle diameters. Compared to the clear water condition, the introduction of solid particles led to a distinct flow separation phenomenon at the backside inlet area of the blade, suggesting degraded cavitation performance. Furthermore, the pressure on the outlet side of the blade's working surface is reduced due to the backflow effect. Across all the investigated solid particle diameters, the pressure trends on both sides of the blades exhibited similar patterns, with higher pressures observed on the front side overall. Specifically, the pressure on the front side gradually decreases along the streamline direction, whereas it gradually increases on the back side. The fluid density under two-phase flow conditions was higher than that under clear-water conditions, resulting in higher pressures on the working surface of the blade in this

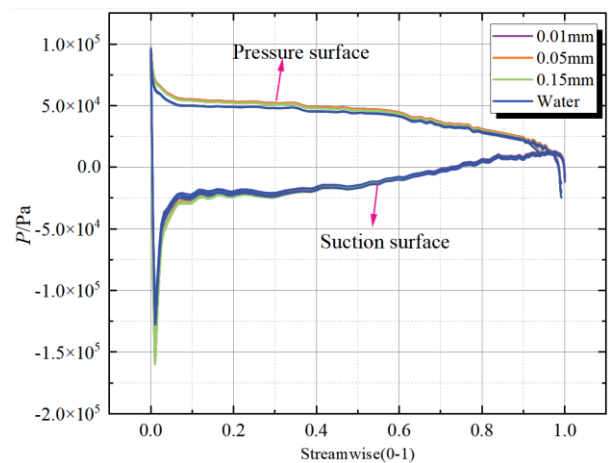


Fig. 6 Pressure distribution along streamline at mid-section of blade

scenario. Moreover, as solid particles enter the blade inlet region and collide with the blade, their velocity diminishes, converting kinetic energy into pressure energy on the blade, leading to a slight increase in pressure. However, with larger solid particle diameters, the energy loss due to collisions increases, significantly hindering fluid flow and causing more pressure drop losses during the flow process. Furthermore, larger solid particle diameters exacerbate friction losses within the channel, reducing the energy level of the fluid. Consequently, despite the higher initial pressure energy under two-phase flow conditions, there was a slight decrease in pressure energy with increasing solid particle diameter. The influence of changes in solid particle diameter on the pressure distribution across the blade's back side was relatively limited. In general, under two-phase flow conditions, the pressure differentials between the front and back sides of the blades were more pronounced compared to those observed in clear-water conditions.

Figure 7 illustrates the pressure distribution along the flow direction at the midsection of the impeller blade for different solid particle diameters. Compared to the clear water scenario, the presence of solid particles led to significant flow separation on the pressure side of the

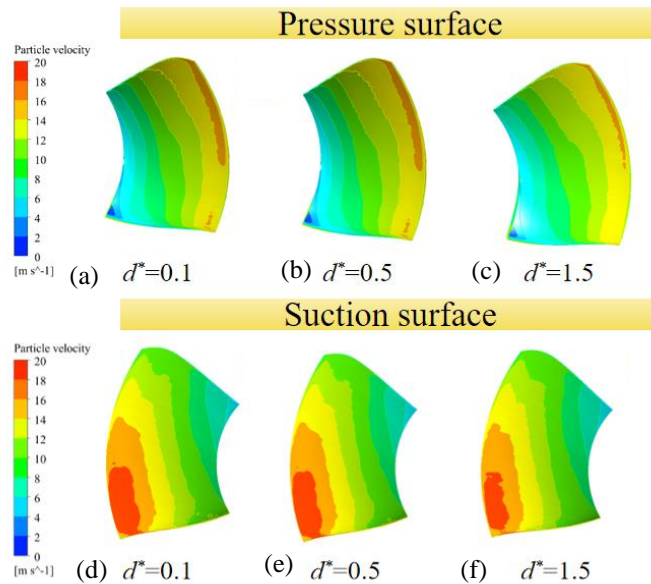


Fig. 7 Distribution of solid particle velocity on blade surface

blade, resulting in reduced cavitation performance. The pressure on the suction side remained relatively low due to recirculation effects. Overall, the pressure trends on both the pressure and suction surfaces were similar across all particle diameters, with the pressure side consistently exhibiting higher pressure values than the suction side. On the pressure surface, pressure gradually decreased along the flow direction, while on the suction surface, it increased. The two-phase flow condition, with a higher density than the clear water case, produced elevated pressures on the blade’s working surface. Moreover, introducing solid particles into the impeller reduced their velocity upon collision with the blade inlet, converting kinetic energy into pressure energy, leading to a slight increase in pressure. As the particle diameter increased, greater energy losses occurred due to collisions, which hindered fluid flow and resulted in higher pressure drops. Larger particle diameters also increased friction losses within the flow passage, further decreasing fluid energy and slightly reducing pressure energy. The variations in particle diameter had little effect on the suction side pressure distribution. Notably, under two-phase flow conditions, the pressure differential between the pressure and suction surfaces was more pronounced than in the clear water case.

Figure 8 shows the distribution of solid particle velocity along the streamline direction near the blade edge. This graph highlights the varying abrasive impacts of the solid particles on the blade surface, with solid particle velocity serving as a critical factor for evaluating abrasive forces. Higher velocities of solid particles correspond to greater kinetic energy, resulting in stronger impacts on the blade surface. A noticeable reduction in velocity occurred at the backside inlet of the blade following collisions between the particles and the surface. In general, there was a gradual decrease in solid particle velocity along the streamline direction, with the peak velocity observed at the leading edge on the inlet side. However, in the middle section, near the blade’s working surface edge, the variation

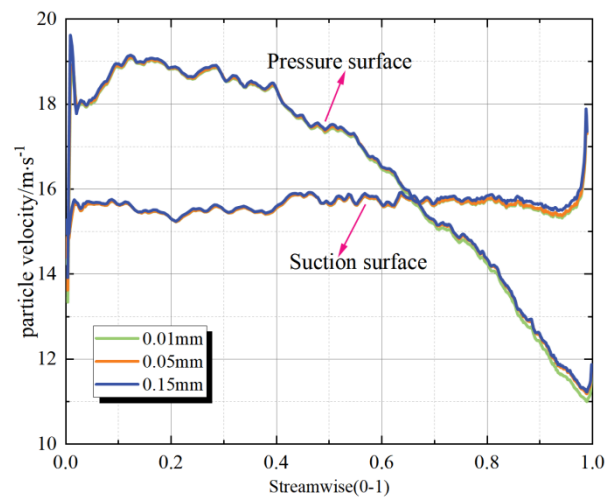


Fig. 8 displays the distribution of solid phase velocity on the blade surface at a span of 0.9

in solid particle velocity was relatively small. At the outlet, a sharp increase in particle velocity was seen due to the centrifugal forces exerted by the runner. Additionally, the analysis revealed that particle size had an impact on the slip velocity of the solid particles. As the particle diameter increased, a slight upward trend in the solid particle slip velocity was observed, particularly near the blade exit.

Figure 9 illustrates the distribution of solid particle concentration on the blade surface for varying solid particle diameters. In general, the concentration of solid particles on the blade’s backside was markedly higher than that on the working surface. Under different particle diameter conditions, the distribution of solid particles on the blade surface displayed nonuniformity, which became more pronounced as the diameter increased. Both the front and back solid particle distributions exhibited a similar trend, decreasing from the hub toward the rim. High-

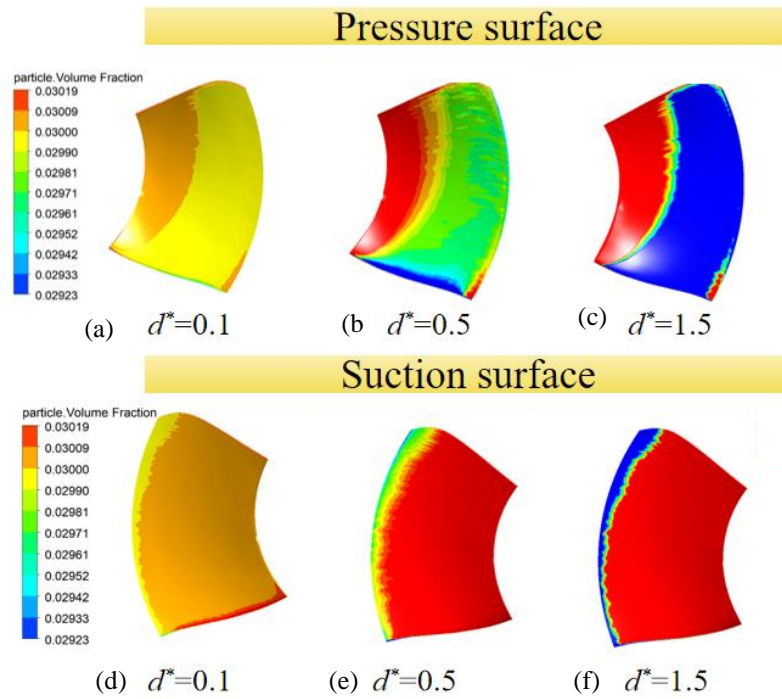


Fig. 9 Distribution of solid particle concentration on blade surface

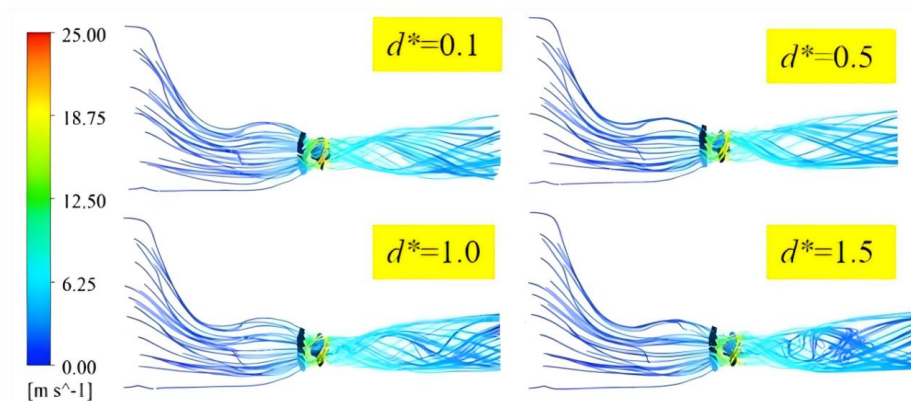


Fig. 10 Particle trajectories at different diameters of solid phase

concentration regions on the front side were clustered near the hub and inlet, while the backside showed higher overall solid particle concentration, with low-concentration areas located close to the blade edge.

As the solid particle diameter increased, a low-concentration zone appeared near the blade edge on the working surface, gradually expanding in size. Simultaneously, the high-concentration regions at the hub and the leading edge of the inlet side became more prominent. Analysis of the solid particle velocity distribution on the blade revealed that near the hub on the working surface, where velocities were lower, smaller particles adhered more effectively to the liquid phase and were less prone to aggregation. In contrast, larger particles exhibited poorer adherence and tended to accumulate near the hub. Toward the leading edge near the outlet, larger particles were more easily ejected from the blade due to inertial and centrifugal forces, resulting in the lowest solid

particle concentration near the blade edge for larger diameters. On the blade's backside, solid particle concentration increased with larger diameters, although a decreasing trend was observed near the blade edge. Further analysis of the solid particle velocity distribution indicated that regions at the leading edge on the inlet side of the front face and near the rim on the backside were more prone to wear due to higher particle concentration and velocity. Additionally, as the solid particle diameter increased, wear severity intensified. This is primarily attributed to the greater inertia of larger particles, which hinders their effective transport by the fluid.

3.2 Particle Movement Patterns in Bulb Tubular Turbines

As illustrated in Fig. 10, the trajectory distribution of the sediment particles in the inlet section was relatively uniform. Sediment particles flowed from the inlet section into the bulbous body. As water entered the periphery of

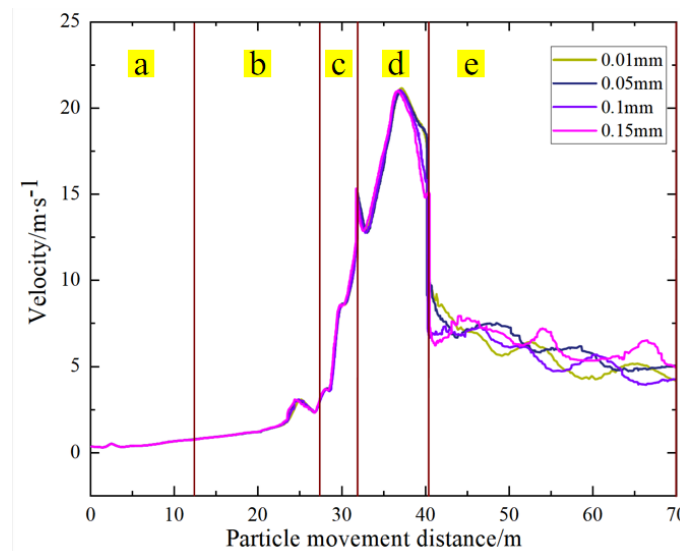


Fig. 11 Particle velocity variation with travel distance at different solid phase diameters

the bulbous body, the velocity of the sediment particles increased slightly owing to the contractive flow passage. When the sediment particles entered the blade channel, they experienced friction and collision with the blades, resulting in energy loss. Upon entering the runner, the solid particles moved closer to the suction surface of the blades. From the trajectory of the sediment particles in the tailwater-pipe region, it is evident that smaller particles exhibit more uniform movement, whereas larger particles display a more chaotic trajectory, generating vortices. The particles entered the guide vane region at a uniform speed along the direction of the water flow. One portion of the particles collided with the surface of the guide vanes, whereas another portion collided with the suction surface of the guide vanes, altering the direction of movement. As the particles entered the runner area, their velocity significantly exceeded that in the guide vane region, transitioning from initial axial movement to rotational movement around the axis. Collisions between the solid particles and suction surface of the blades resulted in changes in the movement direction of the particles. After colliding with the guide vanes and runner blades, the particles entered the tailwater pipe region, where their speed decreased significantly. Near the walls of the tailwater pipe, the particle velocity is higher than that in the central flow region of the tailwater pipe. In the outlet section of the tailwater pipe, as analyzed earlier, a large turbulent zone exists near the wall for larger particle diameters, causing the motion trajectories of the particles to become increasingly chaotic. The collisions among particles, as well as between particles and walls, together with the interactions between particles and fluid, result in pronounced randomness in the tailwater pipe region under conditions with large particle diameters.

Figure 11 illustrates the variation curve of the solid-phase velocity with respect to the distance traveled for different particle diameters moving from the inlet to the outlet of the bulbous tubular hydraulic turbine. It can be observed that the velocity change patterns for different particle sizes are generally consistent, presenting an ‘n’-

shaped trend. Segment ‘a’ shows the velocity variation of the solid phase at the inlet section of the hydraulic turbine, where the initial velocity of the solid phase was set equal to the velocity of the incoming liquid. It is evident that the changes in the solid-phase velocity were relatively small in the inlet section. Segment ‘b’ represents particle velocity within a bulbous body. Because of the contraction at both ends of the exit flow passage, the particle velocity increased. Moreover, larger solid particles have a greater mass and thereby experience stronger inertial forces, resulting in slightly higher velocities compared to smaller diameter particles. Segment ‘c’ is the guide vane region, which directs the water flow and creates circulation. Here, the cross-sectional area decreased further, leading to a significant increase in the solid-phase velocity. In segment ‘d,’ the direction of the particle movement changes within the runner. After colliding with the runner blades, the solid phase experienced a slight velocity reduction owing to energy loss. Subsequently, under the action of the centrifugal force from the turbine, the velocity reaches its maximum at the blade exit. Notably, larger-diameter particles correspond to relatively lower maximum velocities. Beyond this point, the influence of the centrifugal force on the particles diminishes, leading to a marked decrease in particle speed. In segment ‘e,’ within the tailwater-pipe region, when particles enter the conical tailwater pipe, the cross-sectional area continuously increases, which reduces the water flow velocity. At this stage, the water flow velocity significantly affects the solid-phase velocity. Consequently, a general decreasing trend in particle speed is observed within this region. The velocities of the particles fluctuate considerably because they primarily encounter inertial forces after leaving the runner and colliding with the walls of the tailwater pipe. Owing to their greater masses, larger-diameter particles endure larger inertial forces, resulting in more pronounced fluctuations in their maximum speeds.

Figure 12 shows an erosion contour map of the suction surface of the guide vane for different sediment diameters with a sediment concentration of 3%. The figure indicates

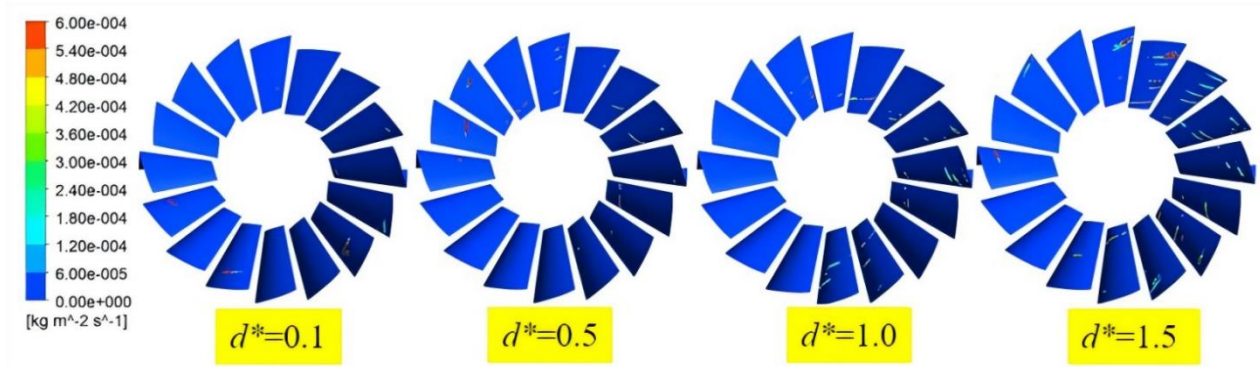


Fig. 12 Erosion contour of the suction surface of the guide vane under different solid phase diameters

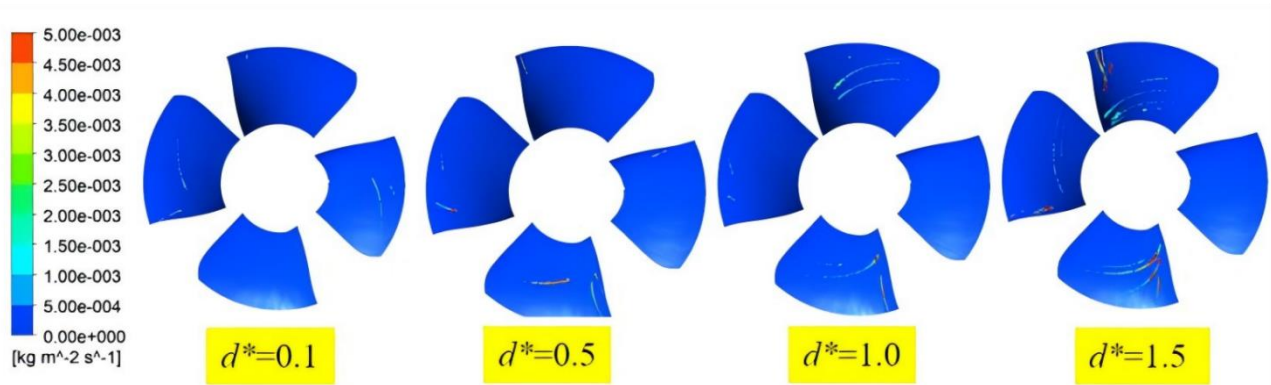


Fig. 13 Erosion contour of the suction surface of the blade suction surface under different solid phase diameters

that as the diameter of the sediment particles increases, the erosion area also expands, transitioning from dot-like erosion at a particle diameter of 0.01 mm to sheet-like erosion at 0.15 mm. As the diameter of the solid phase increases, its inertia also increases, resulting in poorer particle mobility and more frequent collisions with the guide vanes. Consequently, larger solid particle diameters correspond to an increase in the wear area of the guide vanes. It is also noted that the wear levels experienced by the front and suction surfaces of the movable guide vanes differ. As previously analyzed, the solid-phase velocities and their concentration distributions on the suction surface of the movable guide vanes are greater than those on the front surface, leading to less wear on the front. Therefore, the focus of this analysis was primarily on the extent of wear on the suction surface of the movable guide vanes.

Figure 13 shows the wear distribution contour map on the suction surface of the blades for different sediment particle diameters. The wear patterns on the suction surfaces of the blades exhibited similar characteristics for all four sediment diameters. The primary wear on the blade backs was concentrated at the inlet edge near the blade tip and along the midsection in the direction of the flow streamlines. As the particle diameter increased, both the extent of wear and severity of erosion progressively worsened. This is because larger particles possess greater inertia, resulting in poorer fluid followability and increased disorder within the runner; consequently, some particles enter the impeller passages and come into contact

with other particles or the wall surface. These interactions allow them to break away from the constraints of the liquid phase and collide with the suction surfaces of the blades at higher speeds. Regions with higher sediment concentrations gradually shifted towards the rim, leading to observable wear near this area. With the rotation of the runner, the degree of particle aggregation diminished, resulting in a more concentrated wear region at the blade inlet edge while dispersing along the flow streamline direction. Because of the centrifugal force acting on the solid-phase particles, those closer to the rim experience greater forces, making it easier for the sediment to be expelled towards the blade edges. Consequently, wear was observed near the rim for larger particle diameters. Due to the angles of the blades and their twisting, some particles moved from the guide vane outlet to the concave center of the blade front, rotating away from the runner. Meanwhile, many other particles influenced by prerotation directly contacted the inlet side of the back of the blade. The direction of the movement of these particles formed a significant erosion angle with respect to the suction surface of the blade. Depending on the curvature of the blade surface and the direction of rotation, the particles are flung circumferentially by centrifugal force. During this process, the particles maintained a high circumferential velocity, but their relative kinetic energies remained low. Solid-phase particles driven by the high-speed water flow tend to deviate towards the back of the blades, reducing the likelihood of contact with the pressure side of the blades. As previously established, the solid-phase velocities and concentrations on the pressure

side of the blades are lower than those on the back side, leading to less wear on the pressure side. The analysis in Chapter Four highlighted that the inlet region at the back of the blade possesses relatively high solid-phase velocities and unstable flow patterns, making it more susceptible to erosion. Over time, under SLTP flow conditions, the suction side of the blades will exhibit unevenness, causing variations in various hydraulic parameters, which will inevitably lead to a decline in the performance of the hydraulic turbine.

4. CONCLUSION

To examine the hydrodynamic behavior of solid-liquid two-phase (SLTP) flow in a bulb turbine, this study employed an unsteady numerical simulation approach, conducting detailed analyses under various operating scenarios for both clear water and SLTP flow. The simulations provided a comprehensive understanding of the flow dynamics within the bulb turbine across different guide vane openings. Additionally, the relationship between SLTP flow characteristics and the wear of turbine components was investigated. The main findings of the study are summarized as follows:

1) The velocity of the liquid phase on the XY-plane of the bulb turbine exhibited an inverse correlation with the diameter of the solid particles and a direct correlation with the solid concentration. The presence of solid particles heightened the risk of cavitation and vortex formation in the draft tube region, simultaneously leading to a decrease in energy recovery efficiency in this area.

2) The velocity distribution of the solid phase on the runner blade surfaces showed a direct proportionality to the diameter of the inlet solid particles, while the solid concentration on the blade's backside exhibited a positive correlation with both the inlet particle diameter and concentration. With higher inlet solid volume fractions, the solid concentration on the blade's working surface increased. As the diameter of the solid particles grew, the solid concentration at the hub and blade tips increased, whereas it decreased near the edges of the blade.

3) The particle diameter significantly affected the particle trajectory in the tailwater pipe area. Larger-diameter particles exhibited more chaotic movement patterns in this region. The interactions between the particles and fluid led to a high degree of randomness in the particle motion within the tailwater pipe, making it easier for vortices to form. Additionally, the solid-phase diameter had a considerable effect on the solid-phase velocity in the tailwater pipe area. As the particle diameter increased, the solid-phase velocity at the inlet of the tailwater pipe decreased; however, there were larger fluctuations in the velocity within the tailwater pipe region.

Particle shape and density are also important factors that influence the flow characteristics of SLTP flows. While the current study focuses on particle diameter owing to its significant impact, future research should explore the effects of particle shape and density to achieve a more comprehensive understanding of the flow behavior and wear mechanisms in bulb turbines.

ACKNOWLEDGEMENTS

This study was supported by the National Natural Science Foundation of China (52066011), Gansu Province University Teachers Innovation Fund (2023B-434), Key University-level Project (2024XJKXM03), Gansu Province Talent Project (Youth Team) (2024QNTD38), and 2023CA2057 Research on the Modification of Large-Scale Li₂CO₃ Proton Exchange Membrane Fuel Cells for Energy Storage and Demonstration Application Promotion of Talent.

CONFLICT OF INTEREST

The authors declare no conflicts of interest.

AUTHORS CONTRIBUTION

Feng Zhou: Funding acquisition; **Qifei Li:** proofreading, supervision. Simulation; **Qifan Wang:** experiment, data collation, writing-original manuscript. All authors have read and agreed to the published version of the manuscript.

References

- Brezovec, M., Kuzle, I., Krpan, M., & Holjevac, N. (2020). Improved dynamic model of a bulb turbine-generator for analyzing oscillations caused by mechanical torque disturbance on a runner blade. *International Journal of Electrical Power & Energy Systems*, *119*, 105929. <https://doi.org/10.1016/j.ijepes.2020.105929>
- Chen, L., Zhao, Z., Zhang, S., Zhang, S., & Sun, Y. (2019). Effect of particle shape on pipeline damage in liquid-solid two-phase flow. *Journal of Physics: Conference Series*, *1300*(1), 012099. <https://doi.org/10.1088/1742-6596/1300/1/012099>
- Choi, Y. D., & Son, S. W. (2012). CFD analysis on the performance and internal flow of a micro cross-flow hydro turbine in the range of very low specific speed. *The KSFM Journal of Fluid Machinery*, *15*(6), 25–30. <https://doi.org/10.5293/kfma.2012.15.6.025>
- Coulaud, M., Lemay, J., & Deschenes, C. (2020). Experimental study of a bulb turbine model during start-up and at speed-no-load conditions, based on the measurement of unsteady pressure. *Journal of Fluids Engineering*, *142*(8), 081210. <https://doi.org/10.1115/1.4047610>
- Dryden, H. L., Von Karman, T., & Adam, K. A. (2016). *Fluid mechanics and statistical methods in engineering*. University of Pennsylvania Press.
- Fonkenell, J. (2003). Evolution de la technologie des turbines "bulbe" appliquée aux petites centrales. *La Houille Blanche*, *89*(2), 27–31. <https://doi.org/10.1051/lhb/2003027>
- Guénette, V., Houde, S., Ciocan, G. D., J Huang & C Deshenes, S. (2012). Numerical prediction of a bulb turbine performance hill chart through RANS

- simulations. *IOP Conference Series: Earth and Environmental Science*, 15(3), 032007. <https://doi.org/10.1088/1755-1315/15/3/032007>
- Han, W., Chen, Y., Liu, Y., Li, G., Wang, T., Drain, J. (2018a). Numerical simulation of end surface erosion characteristics of a hydro-turbine guide vane. *Journal of Drainage and Irrigation Machinery Engineering*, 36, 404–412. <https://doi.org/10.3969/j.issn.1674-8530.17.0188>.
- Han, W., Chen, Y., Liu, Y., Wei, S., Li, G., Jin, J. (2018b). Prediction of erosional shape evolution in end-surface clearance of turbine guide vane. *Transactions of the Chinese Society of Agricultural Engineering*, 34(4), 100–107. <https://doi.org/10.11975/j.issn.1002-6819.2018.04.012>
- Kang, M. W., Park, N., & Suh, S. H. (2016). Numerical study on sediment erosion of Francis turbine with different operating conditions and sediment inflow rates. *Procedia Engineering*, 157, 457–464. <https://doi.org/10.1016/j.proeng.2016.08.411>
- Lemay, S., Aeschlimann, V., Fraser, R., Ciocan, G. & Deschenes, C. (2015). Velocity field investigation inside a bulb turbine runner using endoscopic PIV measurements. *Experiments in Fluids*, 56, 1–12. <https://doi.org/10.1007/s00348-015-1921-4>
- Li, W., Li, Z., Han, W., Li, Y., Yan, S., Qin, Z., & Chen, F. (2023a). Measured viscosity characteristics of Fe₃O₄ ferrofluid in magnetic and thermal fields. *Physics of Fluids*, 35(1), 012002. <https://doi.org/10.1063/5.012002>
- Li, W., Li, Z., Han, W., Tan, S., Yan, S., Wang, D., & Yang, S. (2023b). Time-mean equation and multi-field coupling numerical method for low-Reynolds-number turbulent flow in ferrofluid. *Physics of Fluids*, 35(12), 125145. <https://doi.org/10.1063/5.0133121>
- Li, W., Li, Z., Han, W., Li, D., Yan, S., & Zhou, J. (2024). Study of the flow characteristics of pumped media in the confined morphology of a ferrofluid pump with annular microscale constraints. *Journal of Fluids Engineering*, 146, 1–31. <https://doi.org/10.1115/1.4056341>
- Li, W., Li, Z., Qin, Z., Yan, S., Wang, Z., & Peng, S. (2022). Influence of the solution pH on the design of a hydro-mechanical magneto-hydraulic sealing device. *Engineering Failure Analysis*, 135, 106091. <https://doi.org/10.1016/j.engfailanal.2022.106091>
- Li, Y., Zhuang, L., & Jiang, Z. (2022). Study of the two-phase flow and wear of a pump with mixed-size particles. *Processes*, 10(3), 565. <https://doi.org/10.3390/pr10030565>
- Li, Z. G., Wang, B., Ma, B., Ou, C., Dong, G., Yang, F., & Li, Y. (2018). The simulation analysis and operation conditions optimization of low-head water bulb tubular turbine based on different guide vane outlet angles. *IOP Conference Series: Earth and Environmental Science*, 163(1), 012008. <https://doi.org/10.1088/1755-1315/163/1/012008>
- Li, Z., Wang, Y., Li, T., Liu, F., & Ji, J. (2019). The dynamic characteristics of the ultimate strength of a turbine runner blade under hydraulic excitation. *Energy Sources, Part A: Recovery, Utilization, and Environmental Effects*, 41(24), 3127–3137. <https://doi.org/10.1080/15567036.2018.1564262>
- Litvinov, I., Shtork, S., Gorelikov, E., Mitryakov, A., & Hanjalic, K. (2018). Unsteady regimes and pressure pulsations in the draft tube of a model hydro turbine in a range of off-design conditions. *Experimental Thermal and Fluid Science*, 91, 410–422. <https://doi.org/10.1016/j.expthermflusci.2017.11.018>
- Pereira, Jr, J. G., Favrel, A., Andolfatto, L., Landry, C., Alligne, S., Nicolet, C., & Avellan, F. (2019). Procedure for predicting part load resonance in Francis turbine hydropower units based on swirl number and local cavitation coefficient similitude. *Mechanical Systems and Signal Processing*, 132, 84–101. <https://doi.org/10.1016/j.ymsp.2019.06.011>
- Thapa, B. S., Thapa, B., & Dahlhaug, O. G. (2012). Empirical modelling of sediment erosion in Francis turbines. *Energy*, 41(1), 386–391. <https://doi.org/10.1016/j.energy.2011.07.024>
- Wilhelm, S., Balarac, G., Métais, O., & Segoufin, C. (2016). Head losses prediction and analysis in a bulb turbine draft tube under different operating conditions using unsteady simulations. *IOP Conference Series: Earth and Environmental Science*, 49(2), 022010. <https://doi.org/10.1088/1755-1315/49/2/022010>
- Xie, G., Li, Q., Xin, L., & Li, Z. (2023). Analysis of solid-liquid two-phase flow in the area of rotor and tailpipe. *Processes*, 11(12), 3382. <https://doi.org/10.3390/pr11123382>
- Yi, S., & Liu, X. (2013). Performance test on solid-liquid two-phase flow hydrotransport of a vortex pump. *Transactions of the Chinese Society of Agricultural Engineering*, 29(22), 76–82. <https://doi.org/10.3969/j.issn.1002-6819.2013.22.009>
- Zhao, Y., Liao, W., Li, Z., Yuan, H., & Luo, X. (2013). Flow field performance of a bulb turbine with C-type or S-type blades. *Transactions of the Chinese Society of Agricultural Engineering*, 29(17), 47–53. <https://doi.org/10.3969/j.issn.1002-6819.2013.17.007>